Geofísica Internacional (2025) **64-2**: 1521- 1531

Geomechanic modeling of seismic emission due to fracture growth - connection to microseismic source mechanisms

Anton A. Duchkov[1], Yury P. Stefanov[1] and Sergey Yaskevich[1]

Abstract

We present an approach to study the rock failure mechanisms due to fracture growth or activation. Our approach includes a series of numerical geomechanic simulations of an incremental rock failure (fracture growth) accounting for elastic wavefield generation and propagation. We then record these wavefields and perform their seismic moment-tensor inversion. We then try to establish connections between seismic moment-tensor solutions and different geomechanic scenarios of the fracture growth with possible applications in monitoring hydraulic fracturing, reservoir development, and local tectonic stress analysis. Our results show that in most cases the amplitudes of generated P-and S-waves can be reasonably well approximated by a moment-tensor point source. When the fracture hits the pre-existing crack then we observe stronger seismic emission compared to the case of the fracture growth in continuous medium. Thus our geomechanic modeling confirms the concept that the most noticeable microseismicity may come from activating the existing natural fractures rather than from the main fracture growth. We also note that the S-wave radiation pattern may be asymmetric (does not correspond to any ideal moment tensor) radiating more energy forward when the fracture hits long pre-existing cracks. Finally, our examples show that the moment tensors may give misleading idea about the direction of the fracture growth (advancement). This result should be kept in mind when interpreting microseismic data in the hydrofrac monitoring applications.

Key words: Microseismic monitoring, seismic moment-tensor inversion, geomechanic modeling, hydraulic fracture.

Resumen

Presentamos un enfoque para estudiar los mecanismos de falla de la roca debido al crecimiento o activación de fracturas. Nuestro enfoque incluye una serie de simulaciones numéricas geomecánicas de una falla incremental de la roca (crecimiento de la fractura) que tiene en cuenta la generación y propagación del campo de ondas elásticas. Luego registramos estos campos de ondas y realizamos su inversión momento-tensor sísmico. A continuación intentamos establecer conexiones entre las soluciones del tensor de momento sísmico y diferentes escenarios geomecánicos del crecimiento de la fractura, con posibles aplicaciones en el monitoreo de la fracturación hidráulica, el desarrollo del yacimiento y el análisis de esfuerzos tectónicos locales. Nuestros resultados muestran que en la mayoría de los casos las amplitudes de las ondas P y S generadas pueden aproximarse razonablemente bien por una fuente puntual del tensor de momento. Cuando la fractura alcanza una grieta preexistente, observamos una mayor emisión sísmica comparada con el caso del crecimiento de la fractura en un medio continuo. Por lo tanto, nuestro modelado geomecánico confirma el concepto de que la microsismicidad más notable puede provenir de la activación de las fracturas naturales existentes en lugar del crecimiento de la fractura principal. También observamos que el patrón de radiación de la onda S puede ser asimétrico (no correspondiente a ningún tensor de momento ideal) irradiando más energía hacia adelante cuando la fractura alcanza grietas mayores preexistentes. Finalmente, nuestros ejemplos muestran que los tensores de momento pueden dar una idea incorrecta sobre la dirección del crecimiento (avance) de la fractura. Este resultado debe tenerse en cuenta al interpretar datos microsísmicos en las aplicaciones de monitoreo de hidrofracturamiento.

Palabras clave: Monitoreo microsísmico, inversión tensor momento sísmico, modelado geomecánico, fractura hidráulica.

Received: May 2, 2024; Accepted: February 5, 2025; Published on-line: April 1, 2025.

Editorial responsibility: Dr. Jonas D. De Basabe

* Corresponding author: Sergey Yaskevich, yaskevichsv@gmail.com
[1] Novosibirsk State University, Novosibirsk, Russia; Trofimuk Institute of Petroleum Geology and Geophysics SB RAS, Novosibirsk, Russia.

Anton A. Duchkov, Yury P. Stefanov, Sergey Yaskevich
https://doi.org/10.22201/igeof.2954436xe.2025.64.2.1804

1. Introduction

Seismic observations are serving as a major source of the current knowledge on tectonic processes in the Earth. The main object of interest is the earthquake: its location and source mechanism are interpreted in terms of global or local geological models. The earthquake location is an answer on the question "where" and acting as a source of the related fault geography. The earthquake mechanism is used as an answer on the question "how" this fault acts. The so-called double-couple (DC) mechanism is the most common interpretation of the analyzed seismic amplitudes. It has a clear physical interpretation of being equivalent to a shear faulting along a plane segment. Moreover the analysis is sometimes reduced to "beach-ball" diagram analysis, when instead of wave amplitudes analysis only the sign of the arrival is analyzed. Many field data results show more general moment tensors with significant non-double-couple (non-DC) components. Such non-DC mechanisms include a cavity collapse in mines (Sıleny and Milev, 2008), and tensile faulting induced by fluid˘ injection in geothermal or volcanic areas (Julian *et al.*, 1998). In some applications one can expect that the non-DC mechanisms should prevail. For example, hydraulic fracture treatment implies a fracture opening which should produce tensile (dipole-type) sources (Sıleny *et al.*, 2009), along with double-couple sources (Nolen-Hoeksema and Ruff, 2001).

Recent years have brought a better understanding of geomechanic processes in the geologic materials including rock deformation and failure (e.g. see Zoback, 2010). Numerical modeling is used for the analysis of deformation and stress field around magma chambers (Currenti and Williams, 2014), for prediction of fracture zones (Maerten *et al.*, 2006) etc. Starting from the classic linear-elastic fracture mechanic models, many complicated geomechanic modeling methods have been developed for simulating the development and propagation of the fracture accounting for the whole complexity of real geologic formations, plastic failures and fluid/rock interactions (Wang *et al.*, 2016; Flekkøy *et al.*, 2002). It is generally accepted that linear fracture geometries are formed in the ductile formations while complex and interconnected discrete fracture networks are formed in more brittle formations. Another crucial aspect is modeling of the main fracture interaction with other natural fracture systems (Zangeneh *et al.*, 2014). Simulation results demonstrate that final fracture-pattern complexity is strongly controlled by anisotropy of in-situ stresses, rock toughness, orientation of the natural fractures and their cement strength (Dahi-Taleghani and Olson, 2011).The complexity of seismic source mechanism is enhanced when main fracture may hit pre-existing fractures resulting in a shear-type displacement as well (Maxwell, 2014). Note that numerical simulations show that the growing fracture may exert enough tensile and shear stresses to re-open even cemented natural fractures (Dahi-Taleghani and Olson, 2011). However, the link between tectonic processes or production practices is complicated and not yet well-understood. Connection between observed earthquakes and models of rock failure is not simple in most practical cases. Recent theoretical developments in both fields (seismic data inversion and geomechanic modeling) require additional effort in establishing a connection between them.

The fluid's role in earthquakes sometimes seems to be underestimated. Laboratory experiments show that the injection fluid viscosity should influence the fracture propagation detectable by acoustic observations, e.g. viscous fluid injection tends to generate thick and planar cracks producing shear-type mechanisms, less viscous fluid results in thin and wavelike cracks producing tensile-type mechanisms (Ishida *et al.*, 2004). A growing amount of seismic data observed for hydraulic fracturing monitoring allows establishing empirical relations between the parameters of seismicity and hydraulic fracture propagation (Warpinski, 2013). Seismic moment-tensor inversion results are also used for constructing the dominant fracture sets that can provide constraints on the rock properties controlling the fracture growth in the reservoir (Baig and Urbancic, 2012). Integrated fracture system simulation, monitoring, and model updating for reservoir development are discussed in detail in (Pettitt *et al.*, 2011; Maxwell *et al.*, 2015).

However, note that seismic moment-tensor inversion is related to radiation pattern analysis which is also affected by media parameters which are seldom taken into account, and the media considered as homogeneous and isotropic. For example, the radiation pattern may be considerably influenced by seismic anisotropy in the area of the source (Psencık and Teles, 1996), the so-called directivity effect caused by unilaterally rupturing fault (Lay and Wallace (1995), also see the review by Julian *et al.* (1998)). Shi and Ben-Zion (2009) consider radiation patterns for the cases of the similar and dissimilar solids on the sides of the fault and, with numerical modeling, analyze radiation patterns and their possible interpretation in terms of source mechanism. Many potential distorting factors should be taken into account during geologic interpretation of the seismic inversion results. The problem of connecting effective seismic moment tensors to actual seismic emission from the rock failure was first addressed by Loginov *et al.* (2016). Here we consider it in more details.

In this paper we perform a numerical geomechanic modeling of different scenarios of the incremental fracture growth based on the elastic-plastic model of the rock deformation and failure in the form of the fracture growth. This modeling includes the generation and propagation of elastic waves. These waves are analyzed in order to approximate them by an effective point seismic source that is a natural interpretation of the observed

seismic events. These results will be used for connecting the geomechanic models of fracture propagation to the moment tensors that can be retrieved from a seismic data.

2. Theory

2.1. Geomechanic modeling of incremental fracture growth

Our numerical study consisted of two stages. First, we simulated the numerical modeling of the fracture growth. Second, we performed the seismic moment tensor inversion for the generated wave amplitudes.

In this paper we consider a 2D numeric geomechanic model of the incremental fracture growth accounting for generation and propagation of elastic waves caused by the material failure, i.e. seismic emission. For this we use a popular elastic-plastic model (Drucker and Prager, 2013; Nikolaevskii, 1971). Thus we solve the equations of continuity and motion:

$$\frac{d\rho}{dt} + \rho\dot{u}_{i,i} = 0; \quad \sigma_{ij,j} + \rho F_i = \rho\frac{d\dot{u}_i}{dt}, \qquad (1)$$

where ρ - density, $\dot{u}_i$ - velocity-vector components (time derivative of the displacement vector with components u_i), F_i - mass forces, σ_{ij} - components of the Cauchy stress tensor which can be represented as $\sigma_{ij} = -\sigma\delta_{ij} + s_{ij}$ using the spherical stress $\sigma = -\sigma_{kk}/3$, and the deviatoric stress s_{ij} (where δ_{ij} is the Kronecker delta); the index after a comma stands for the derivative.

The strain rate consists of the elastic and plastic parts:

$$d_{ij} = d^e_{ij} + d^p_{ij}. \qquad (2)$$

Then we determine the elastic stresses using the hypo-elastic law:

$$\frac{Ds_{ij}}{Dt} = 2\mu(d^e_{ij} - \frac{1}{3}d^e_{kk}\delta_{ij}), \quad \dot{\sigma} = -K\frac{\dot{V}}{V}\ , \qquad (3)$$

where $Ds_{ij}/\mathrm{D}t = \dot{s}_{ij} - s_{ik}\dot{\omega}_{jk} - s_{jk}\dot{\omega}_{ik}$ is the co-rotational Jaumann derivative which takes into account possible rotation of the material elements, K and μ are the bulk and shear modules respectively; dot above the variable denotes the time derivative; V is the relative volume.

The strain rate tensor d_{ij} and the rotation rate tensor ω_{ij} are determined from the relations:

$$d_{ij} = (\dot{u}_{i,j} + \dot{u}_{j,i})/2, \quad \dot{\omega}_{ij} = (\dot{u}_{i,j} - \dot{u}_{j,i})/2. \qquad (4)$$

We use the modified relations of the Drucker-Prager-Nikolaevskii model (Drucker and Prager, 2013; Nikolaevskii, 1971) as described in (Stefanov *et al.*, 2011). This approach allows for a correct description of the deformation dynamics of elastic as well as elasticplastic media. When the stresses reach the yield surface $f = 0$ then it is necessary to compute the inelastic (or plastic) part of the strain tensor:

$$d^p_{ij} = \lambda\frac{\partial g}{\partial s_{ij}}, \qquad (5)$$

where λ is a non-negative multiplier defined during deformation, $f = \tau - \alpha\sigma - Y$ is the yield-surface function, $g = \tau - \beta\sigma$ is the plastic potential, $\tau = \sqrt{s_{ij}s_{ij}}/2$ is the equivalent shear stress, α is the coefficient of internal friction, β is the dilatancy coefficient, Y is the cohesion.

The numerical model in this work is based on a 2D plane formulation. An explicit numerical finite-difference scheme is used for solving the system of dynamic elastoplastic equations described above, cf. (Wilkins, 1999). We describe the elementary fracture growth explicitly by an incremental advancement with the release of new surfaces by splitting nodes of the computational grid (Wilkins, 1999; Nemirovich-Danchenko and Stefanov, 1995; Stefanov, 2008). We chose this approach as it is well suited for describing a fracture opening by different mechanisms including tensile and shear types.

In our numeric studies we considered only a single advancement act of the fracture. Note that instantaneous incremental crack growth creates high-frequency vibrations taking the form of undesired numerical dispersion in the finite-difference scheme. In order to resolve this issue we remove stresses at progressing fracture increments not instantly but smoothly. This procedure has the effect of a fracture growth in terms of one step of the grid (a similar problem occurs when modeling continuous fracture propagation as a series of elementary advancements). Note that the duration of the smooth stress relief will affect an eventual form of generated seismic emission pulse. Thus, we can adjust the pulse period so that it is suitable for the chosen numerical scheme. Some minimal artificial viscosity is still used to get wavefield records clean enough to study the effect of confining stresses, and the fracture growth scenarios on seismic emission. Numerical wavefields are then recorded

in the far field of the fracture tip so that they simulate seismic waveforms.

2.2. Processing of generated wavefields

The next stage is to mimic seismic data processing and inversion procedures. In this paper we consider the moment-tensor inversion for seismic source mechanism Aki and Richards (2002). Let us consider the 2D case. Then the moment tensor **M** is a symmetric 2 by-2 matrix which can be represented by a vector of three independent entries: $\mathbf{m} = (M_{11}, M_{22}, M_{12})$. This moment tensor describes a point source generating the following wavefield in homogeneous medium:

$$u_i = M_{kl} G_{ik,l}, \quad G_{ik,l} = \frac{g_i g_k n_l}{4\pi\rho v^3 r}, \tag{6}$$

where u_i are the displacement-vector components corresponding to the recorded wavefield, n_i are components of the unit vector **n** directed from the source to the receiver, G_{ij} are components of the Green's tensor, g_i and v are the polarization vector and seismic velocity correspondingly (different for P- and S-waves), and r is the distance between the source and the receiver.

Now for a chosen wave type (P or S) we introduce the so-called radiation pattern describing differences in the wave amplitude radiated from the source in different directions (Psencık and Teles, 1996):

$$R(\mathbf{n}) = g_k n_l M_{kl} / v^3 \tag{7}$$

Eq. (6) defines a linear relation between the recorded wavefield (amplitudes) and the moment-tensor source description:

$$\mathbf{u} = \mathbf{A}\mathbf{m}, \tag{8}$$

where **u** is a vector of amplitudes of the corresponding wave type, matrix **A** depends on the medium properties and the radiation pattern, unknown vector **m** describes the moment-tensor source.

Thus seismic moment tensor at the source can be found as a regularized solution of the system (8). In the inversion examples below we find the least-squares solution to this system. In a more general case (heterogeneous medium, unknown velocities etc.) one can formulate the seismic moment-tensor inversion as an optimization problem by fitting synthetic waveforms to the recorded ones.

3. Numerical Tests

In this section we will show the results of a series of numerical simulations of different scenarios of the incremental fracture growth. Associated seismic emission is then compared to the tensor-moment solutions as suggested in (Loginov *et al.*, 2016).

The model of the incremental fracture growth as schematically shown in Figure 1,A. The main fracture extends from the bottom up with its tip being in the center of the computational domain. In all simulations we consider homogeneous material with the following properties: density is 2.5 kg/cm^3, P-wave velocity is 6 km/s, and S-wave velocity is 3.34 km/s, $Y = 15$ MPa, $\alpha = 0.5$, $\beta = 0.2$. We assume fluid inside the fracture in case of its opening, i.e. there is no material with altered properties but pressure is applied to the fracture surface as a boundary condition.

Confining stress (emulating regional stress field) was applied at the boundaries (as schematically shown in Figure 1,A). In all experiments 40 MPa normal stress was applied to the side boundaries, while 60 MPa normal stress was applied to the top and bottom boundaries (so that the main fracture is aligned with the maximum normal stress direction). In some of the experiments we also applied the shear stress to the side boundaries (10 and 30 MPa). The fracture growth may take place in a continuous homogeneous medium or it may hit a preexisting co-linear crack of length L. Generated elastic wavefields are recorded on a circular profile centered at the main fracture tip. The radius (150 or 200 m) is chosen so that the profile is in the source far field, i.e. P- and S-waves are formed and well separated.

All scenarios of the main fracture advancement include its incremental growth to the length δ (see Figure 1,A). This growth may have a tensile-type mechanism caused by a pressure inside the main fracture (mimics hydro-fracturing). Corresponding radiation patterns of P- and S-waves are shown in Figure 1,B (dipole-type source). Alternative scenario of the fracture growth is a shear-type mechanism caused by the boundary shear stress (mimics fault activation). Corresponding radiation patterns of P- and S-waves are shown in Figure 1,C (double-couple source).

In Figure 2, left we show the elastic wavefield generated by the main fracture incremental growth ($\delta = 3$ m) due to tensile opening in continuous medium (no pre-existing crack). One can see traces from 100 receivers placed on the circular profile: radial displacement velocity component (with respect to the main fracture tip) is shown in the top panel, transversal component – in the bottom panel. The horizontal axis shows the receiver angle on the circle (measured from the vertical axis so that the profile crosses the main fracture at angle π). One can see the P- and S-waves on the radial and the transversal components correspondingly. Central traces clearly contain the Rayleigh wave propagating along the walls of the main fracture. Particle

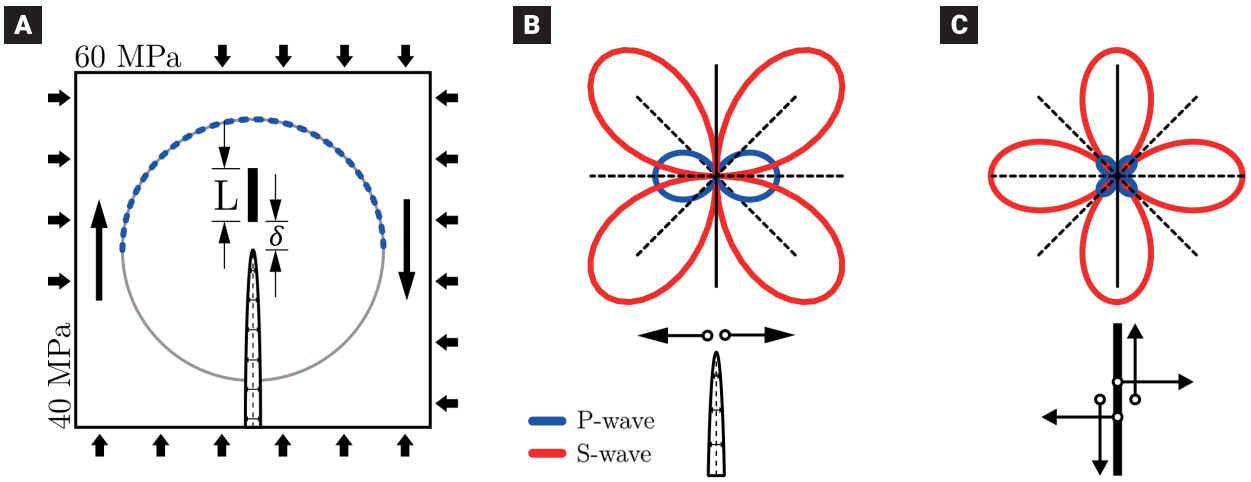

Figure 1. Fracture elementary growth scenarios. A) – geomechanic modeling domain, main fracture and possible pre-existing crack in front of it, arrows show the confining stresses, grey circular – receiver profile, blue dotted half-circle – receiver line used for the moment-tensor inversion; B) – radiation pattern for tensile fracture opening; C) – radiation pattern for shear-type fracture growth. P-wave – blue, S-wave – red.

motion trajectories (hodograms) are shown in Figure 2, right. Trajectories of the particle motion for P-wave are shown in blue (they correspond to the time interval of P-wave shown by blue horizontal lines in Figure 2, left); trajectories for S-waves are shown in red (correspond to the time interval of S-wave shown by red horizontal lines in Figure 2, left). One can see that the polarization of both waves is close to linear which is expected for a point source in elastic medium.

As mentioned earlier while modeling the main fracture incremental growth at distance δ we disconnect nodes of the computational grid but we release the new fracture borders continuously with some prescribed speed. In Figure 3 we show the results of using different border release speed.

Now we consider the same fracture advancement $\delta = 3$ m but different border release speed, as shown in Figure 3. Right panels correspond to the release speed 4 times faster than for traces in the left panels. One can see that faster fracture opening generates waves with higher amplitudes and shorter signal periods. Here we get the P-wave wavelength about 30 m for the data in Figure 3, left and about 15 m for Figure 3, right. Then we pick P-wave amplitudes as the maximum absolute values of the radial component within the P-wave time interval (blue lines in Figure 3); S-wave amplitudes are picked on the transversal component within the S-wave time interval (red lines in Figure 3). Corresponding radiation patterns are shown in Figure 4: blue - for P-waves, red - for S-waves. They show absolute values of waves radiated in all directions assuming that they were generated by a point source located at the fracture tip. One can see that faster border release produces stronger waves but overall shape of the radiation pattern is similar. Thus for further experiments we choose the border release speed which produces cleaner traces (without oscillating numeric dispersion).

Now let us consider the case when advancing fracture breaks the 'bridge' towards preexisting small crack as schematically shown in Figure 1. In Figure 5 we show the radiation patterns for the fracture tensile opening in the case normal boundary stresses; blue lines – P-wave; red lines – S-wave. Three model results are shown: no pre-existing crack (A); pre-existing crack of length 10 m (B); crack of length 20 m (C).

Let us make a few observations from these results. Note that in most cases the S-wave radiation pattern differs from the ideal one known for the dipole point source (cf. Figure 1). Fracture incremental growth in continuous medium results in more S-wave energy radiated back toward the fracture origin (Figure 5,A). This may be an effect of the fracture walls during the wave formation in the near-zone of the source. Stronger waves are generated when the main fracture hits a pre-existing crack. Moreover, the radiation patters changes. Now more energy of the S-wave is emitted forward, i.e. in the direction of the fracture growth. One can see that for some crack length the radiation pattern starts resembling the ideal dipole source (Figure 5,B); then it becomes non-symmetric again (Figure 5,C), note the similar analytical observation in Aki and Richards (2002, Chapter 10, Figure 10.20). Also note that the horizontal orientation of the dipole derived from the radiation pattern coincides with our expectations of the tensile opening of the fracture.

Now we consider the case the shear boundary stress added to the normal boundary stress and the tensile mechanism of the fracture growth. Corresponding radiation patterns are shown in Figure 6 for the shear boundary stresses of 10 MPa (bottom

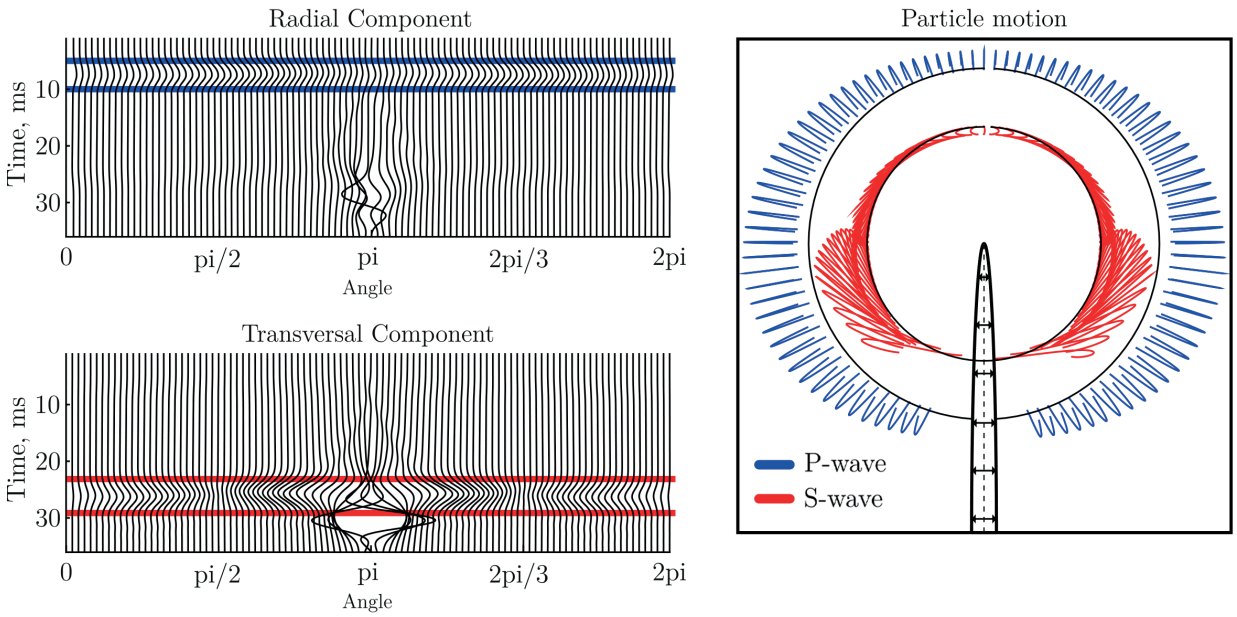

Figure 2. Elastic wavefield generated by the fracture tensile opening (no pre-existing crack, normal boundary stresses). Left: wavefield recorded on the circular line (cf. Fig.1), radial component of particle velocity - top panel, transversal component - bottom, windows of polarization analysis are shown for P-wave (blue lines) and S-waves (red lines). Right: particle motion trajectories for the time intervals of P-wave (blue) and S-wave (red).

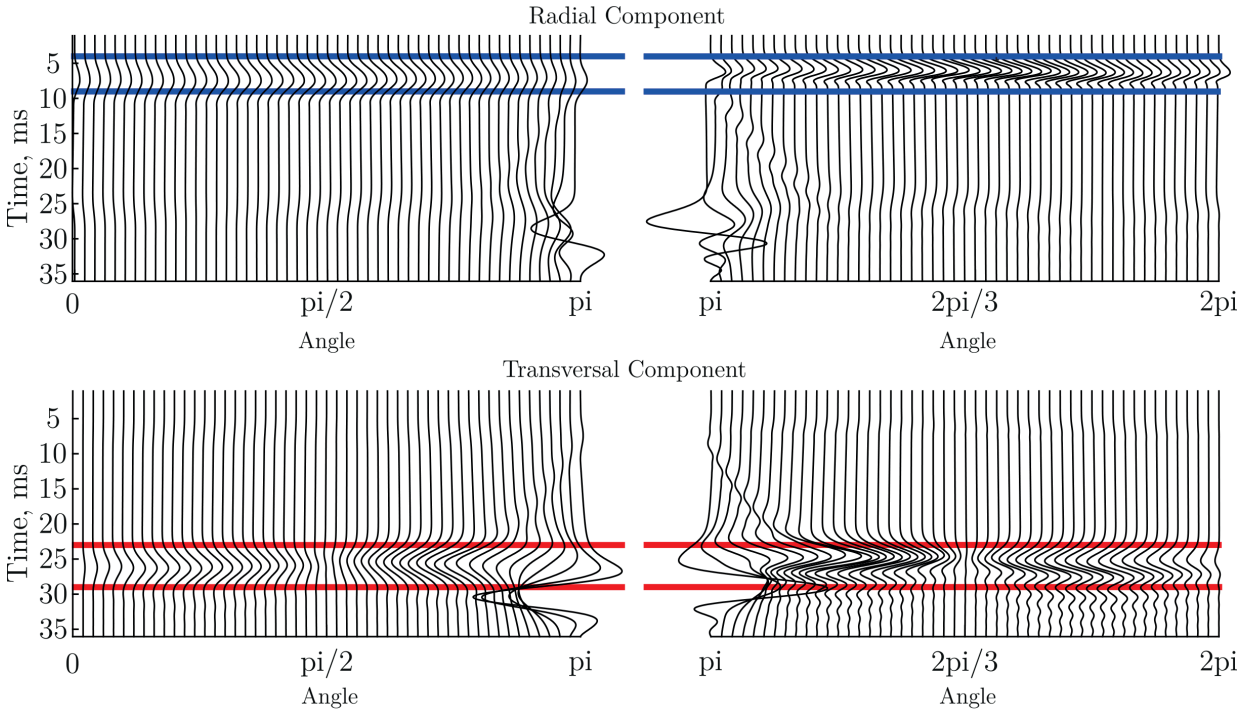

Figure 3. Elastic wavefield generated by the fracture tensile opening with a different speed (no pre-existing crack, normal boundary stresses) and recorded on the circle from Figure 1; top – radial component; bottom – transversal component. Left: slow opening speed; right: fast opening speed.

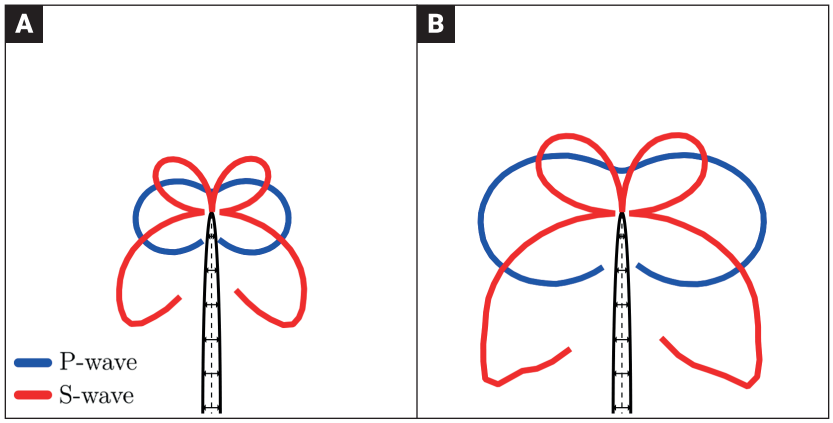

Figure 4. Radiation patterns for the fracture tensile opening with a different speed (no pre-existing crack, normal boundary stresses); blue – P-wave; red – S-wave. Left: slow opening speed; right: fast opening speed.

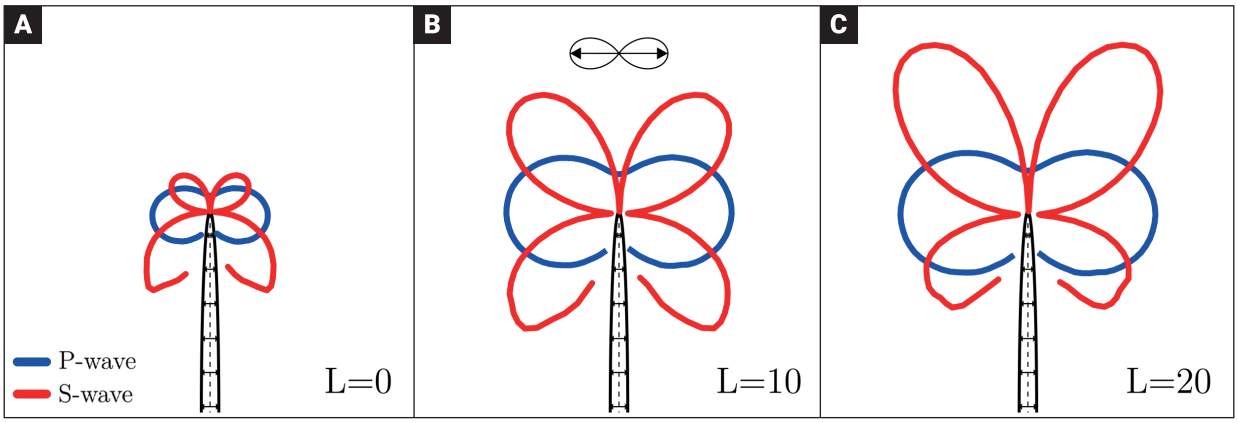

Figure 5. Radiation patterns for the fracture tensile opening in case of pre-existing cracks of different length (normal boundary stresses); blue – P-wave; red – S-wave. A) – no pre-existing crack; B) – crack of $L = 10$ m; C) – crack of $L = 20$ m.

row) and 30 MPa (top row). As usual, blue lines correspond to P-waves, red lines – to S-waves. Note that at the boundaries we now add shear stresses (at the sides) to the normal stresses (cf. Figure 1). Thin lines show orientations of the principal stresses of the resultant stress field. Columns in Figure 6 correspond to different length of the pre-existing crack: no crack (left), $L = 10$ m (middle), $L = 20$ m (right).

In Figure 6 one can see that the intensity of generated waves increases when value of the shear stress increases (from the bottom up) or length of the pre-existing crack increases (from left to right). In the panels we also show how the P-wave radiation pattern can be interpreted in terms of the dipole sources (the S-wave radiation pattern is more complicated and deviates more from the ideal patterns). Note that small shear stress rotates the stress orientations. And the radiation patterns derived from seismic waves correspond to the rotated dipole aligned with these stresses instead of the fracture growth direction (Figure 6, bottom row). For larger boundary shear stress the stress orientations are rotated even more. The P-wave radiation patterns are still aligned with these directions but they are do not look like corresponding to a pure dipole type (Figure 6, top row). They start looking like a rotated double dipole source which will further transform into a double-couple source for even stronger boundary shear stresses.

Then we consider pure-shear rock failure at the fracture due to 30 MPa shear boundary stress (no pressure in the fracture, the same normal boundary stresses). Radiation patterns corresponding to different length of the pre-existing crack are shown in Figure 7: no crack (left), $L = 10$ m (middle), $L = 20$ m (right). As usual, blue lines correspond to P-waves, red lines – to S-waves. Note that the S-wave radiation pattern is asymmetric

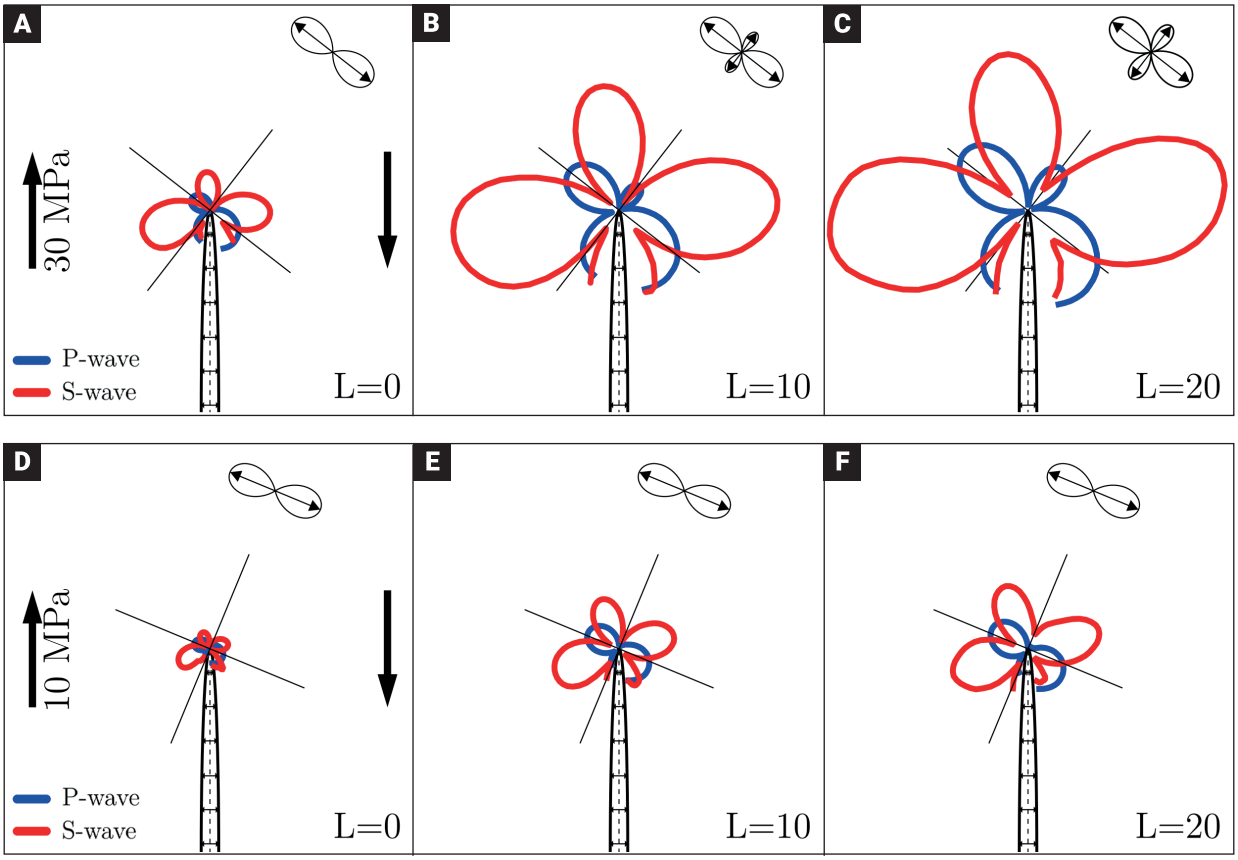

Figure 6. Radiation patterns for the fracture tensile opening in case of additional shear boundary stresses of 10 MPa (bottom row) and 30 MPa (top row). Columns correspond to different length of the pre-existing crack: no crack (A, D), L = 10 m (B, E), L = 20 m (C, F). Thin lines – principal stress orientations due to boundary stresses. P-wave – blue, S-wave – red.

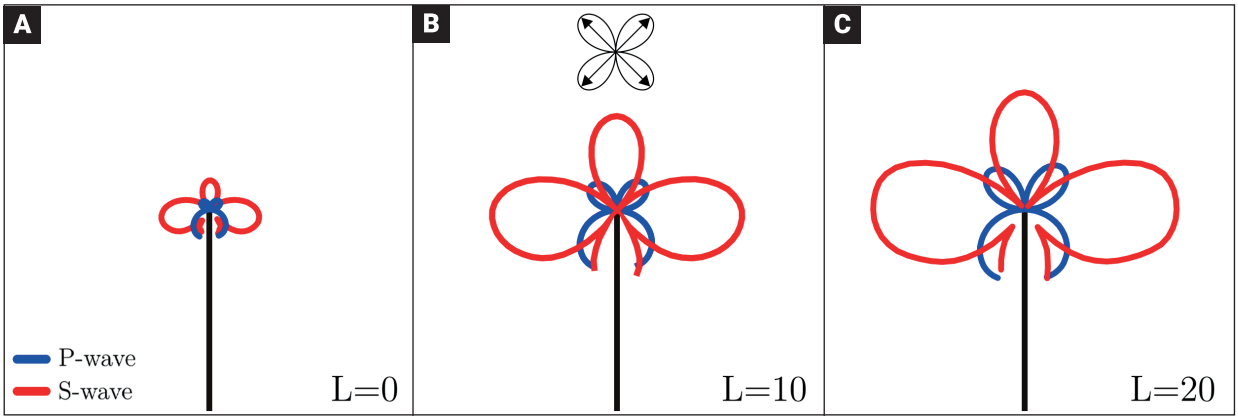

Figure 7. Radiation patterns for the fracture shear-type development (no pressure in frac-ture, 30 MPa shear boundary stress) for different lengths of pre-existing crack: no crack (A), L = 10 m (B), L = 20 m (C). P-wave – blue, S-wave – red.

and differs from the ideal double-couple source (Figure 1,C). With the increasing length of the pre-existing crack we see the increasing intensity of generated waves and the S-wave radiation pattern becomes less asymmetric.

Finally we applied the seismic moment-tensor inversion (SMTI) to the picked P- and S-wave amplitudes. In order to avoid influence of the Rayleigh wave propagating along the fracture we consider restricted aperture of the acquisition array shown by dashed blue line in Figure 1 (upper half-circle). We present the inversion results in Figure 8. Solid lines show the radiation patterns from our geomechanic modeling, dashed lines – the moment-tensor inversion. Panels correspond to different scenarios of the fracture growth.

One can see that overall the radiation pattern observed from geomechanic modeling can be reasonably well approximated by a moment-tensor point source. Inversion results fit the P-wave radiation pattern almost perfectly. Some misfit can be seen for the S-wave radiation pattern in the case of considerable shear boundary stress (30 MPa). In this case the modeling result show stronger S-wave radiation in the direction orthogonal to the main fracture compared to the forward direction (note that the ideal double-couple mechanism produces symmetric sectors of the S-wave radiation pattern, cf. Figure 1,C).

First we consider the tensile fracture opening in the case of normal boundary stresses, and the pre-existing crack of length $L = 10$ m (Figure 8,A). The moment-tensor inversion gives us the radiation pattern which is very close to the theoretical dipole-type source (cf. Figure 1,B) which is a natural mechanism for this case. The dipole orientation perfectly identifies the fracture growth direction (should be orthogonal to the dipole orientation). Then we consider the tensile fracture opening in the case of small shear boundary stress (10 MPa), and the pre-existing crack of length $L = 20$ m (Figure 8,B). Note that the source mechanism still looks very much like a dipole but it is oriented at an angle of 22° from the horizontal. Thus the dipole source orientation provides false information if it is in-

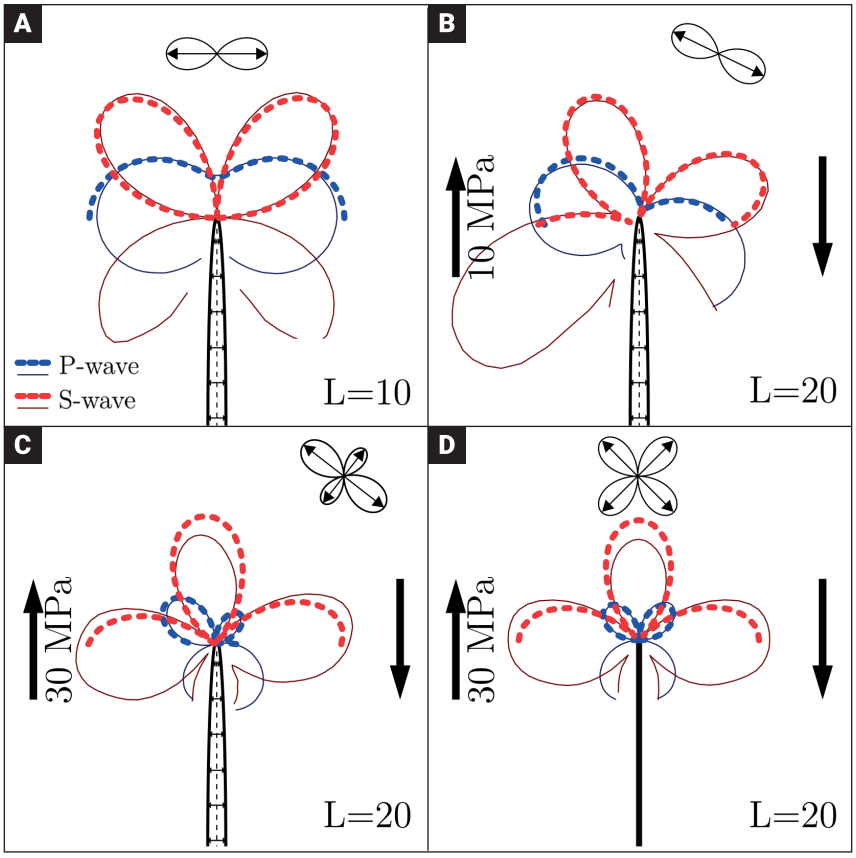

Figure 8. Seismic moment-tensor inversion results for different models; solid line – radiation pattern from geomechanic modeling, dashed line – the moment-tensor inversion result. Different scenarios of the fracture growth: tensile opening, only normal boundary stresses, pre-existing crack of $L = 10$ m (A); tensile opening, 10 MPa shear boundary stress, pre- existing crack of $L = 20$ m (B); tensile opening, 30 MPa shear boundary stress, pre-existing crack of $L = 20$ m (C); shear-type growth (no pressure in fracture), 30 MPa shear boundary stress, pre-existing crack of $L = 20$ m (D). P-wave – blue, S-wave – red.

terpreted as showing the fracture growth direction (corresponds to the principal stress directions). Next we consider the tensile fracture opening in the case of stronger shear boundary stress (30 MPa), and pre-existing crack of $L = 20$ m (C) (Figure 8,C). Note that the P-wave radiation pattern now corresponds to two orthogonal dipoles of different intensity oriented at an angle of 37° from the coordinate axes. The S-wave radiation pattern is not fitted perfectly and it exhibits asymmetry of radiation discussed earlier for the shear-type mechanism. Note that now the tensile nature of the fracture opening is somewhat masked in the source mechanism and its orientation is not showing the fracture growth direction. Finally, we consider the shear-type fracture development in the case of shear boundary stress (30 MPa), and pre-existing crack of $L = 20$ m (C) (Figure 8,D). Note that the P-wave radiation pattern is well fitted by the double-couple mechanism, while the S-wave radiation pattern is not fitted perfectly and it exhibits asymmetry of radiation discussed earlier for the shear-type mechanism. Also note that if this mechanism is interpreted as a double-couple (cf. Figure 1,C) then its orientation is in good correspondence with the fracture growth direction.

4. Conclusions

This study explores the limits of seismic monitoring's theoretical ability to resolve rock failure mechanisms associated with fracture growth or activation. Our approach includes numerical geomechanic modeling of incremental rock failure (fracture growth) accounting for elastic wavefield generation and propagation. We record this wavefield and perform its seismic processing (seismic moment-tensor inversion). In this way we get effective point-source mechanisms which can be associated with earthquakes observed during fracture propagation.

Then we try to establish connections between the moment tensor solutions and different geomechanic scenarios of the fracture development. For this we carry out numerical geomechanic simulations corresponding to different scenarios of elementary fracture growth (small advancement step): different fracture growth mechanisms (tensile and shear), different types of boundary stress (only normal stress, normal and shear stresses), interaction with pre-existing cracks. We then check if these scenarios can be identified from elastic waves recorded in a far field of the source.

In general, amplitudes of generated elastic waves can be reasonably well approximated by moment-tensor point sources. Especially for the tensile-type fracture growth (fracture opening due to excessive pressure in it) we usually get radiation patterns corresponding to dipole-type source mechanisms which is in good agreement with the theory.

Let us sum up a few more observations. Note that when the fracture hits a pre-existing crack then stronger waves are generated compared to the fracture growth in continuous medium. Thus our modeling confirms the concept that the fracture growth itself may take place without producing much seismicity while noticeable earthquakes may be generated when the main fracture hits pre-existing cracks and faults (cf. Maxwell (2014)). However, we have got some new observation about the shape of the radiation patterns in this case. We noted that for the tensile fracture growth in homogeneous medium there is more S-wave energy radiated backward (towards the fracture beginning). For the fracture hitting the pre-existing crack we see some compensation of this effect. So that the radiation of the S-wave forward increases with the increasing length of the pre-existing crack. Thus at certain crack size the S-wave radiation pattern appears to be close to the theoretical one for the dipole source (tensile fracture opening).

Note that the described asymmetries in the radiation patterns may cause distortions in the magnitude estimations depending on the acquisition design. Also note that there are other sources of such asymmetries discussed in the introduction. We hope that it is possible to distinguish between these different sources. For example, the influence of seismic anisotropy is reported to have stronger affect on the P-wave radiation pattern (cf. Psencık and Teles (1996)) while our experiments show that the S-wave radiation pattern is affected more. The directivity effect from rupturing fault (Lay and Wallace, 1995) results not only in the distortion of the radiation pattern, but the signal period should be also different in different directions. We do not see such signal variability in our data.

Finally, our examples show that seismic moment-tensors may give a completely wrong estimation of the direction of the fracture growth (advancement). Inverted mechanisms of the dipole type are usually associated with the fracture tensile opening (being orthogonal to the fracture advancement direction). But the dipole orientation may differ considerably from the fracture growth direction in presence of shear boundary (regional) stresses. This result should be kept in mind when interpreting seismic data.

We hope that further studies will help establishing better connections between geomechanic models of rock failure and the inversion of seismic data. Then the seismic observation may be successfully used for calibrating geomechanic models with applications in monitoring hydraulic fracturing, reservoir development and regional tectonic processes.

5. Acknowledgments

The study was carried out with financial support support of the Russian Federation represented by the Ministry of Science and Higher Education through grant 075-15-2003-588.

6. References

Aki, K., and P. G. Richards. (2002). Quantitative seismology. University Science Books

Baig, A. M., and T. I. Urbancic (2012). Towards using seismic moment tensor inversions to infer reservoir rock properties. [Conference paper]. 74th EAGE Conference and Exhibition incorporating EUROPEC.

Currenti, G., and C. A. Williams. (2014). Numerical modeling of deformation and stress fields around a magma chamber: Constraints on failure conditions and rheology. Physics of the Earth and Planetary Interiors, 226, 14–27. doi: **https://doi.org/10.1016/j.pepi.2013.11.003**

Dahi-Taleghani, A., and J. E. Olson. (2011). Numerical modeling of multistranded-hydraulicfracture propagation: accounting for the interaction between induced and natural fractures. SPE Journal, 16(03), 575–581. doi: **https://doi.org/10.2118/124884-PA**

Drucker, D. C., and W. Prager. (2013). Soil mechanics and plastic analysis or limit design. Quarterly of Applied Mathematics, 10.

Flekkøy, E. G., A. Malthe-Sørenssen, and B. Jamtveit. (2002). Modeling hydrofracture. Journal of Geophysical Research Solid Earth, 107(B8), 1-11. doi: **https://doi.org/10.1029/2000JB000132**

Ishida, T., Q. Chen, Y. Mizuta, and J.-C. Roegiers. (2004). Influence of fluid viscosity on the hydraulic fracturing mechanism, Journal of Energy Resources Technology, 126(3), 190–200. doi: **https://doi.org/10.1115/1.1791651**

Julian, B. R., A. D. Miller, and G. Foulger. (1998). Non-double-couple earthquakes 1. Theory. Reviews of Geophysics, 36(4), 525–549. doi: **https://doi.org/10.1029/98RG00716**

Lay, T., and T. C. Wallace. (1995). Modern global seismology. Academic Press.

Loginov, G., A. A. Duchkov, and Y. P. Stefanov. (2016). Numeric study of resolvability of rock-failure mechanism from seismic moment-tensor inversion. SEG Technical Program Expanded Abstracts, SEG, 2564–2568. doi: **https://doi.org/10.1190/segam2016-13972264.1**

Maerten, L., P. Gillespie, and J.-M. Daniel. (2006). Three-dimensional geomechanical modeling for constraint of subseismic fault simulation. AAPG Bulletin, 90(9), 1337-1358. doi: **https://doi.org/10.1306/03130605148**

Maxwell, S. (2014). Microseismic imaging of hydraulic fracturing. Society of Exploration Geophysicists.

Maxwell, S., D. Chorney, and S. Goodfellow. (2015). Microseismic geomechanics of hydraulicfracture networks: Insights into mechanisms of microseismic sources. The Leading Edge, 34(8), 904-910. doi: **https://doi.org/10.1190/tle34080904.1**

Nemirovich-Danchenko, M. M., and Y. P. Stefanov. (1995). Application of the finite-difference method in lagrange variables to calculation of wave fields in complexly structured media, Russian Geology and Geophysics, 36, 97–111.

Nikolaevskii, V. N. (1971). Constitutive equations for plastic deformation of granular media. J Appl Math Mech, 6, 1070–1082.

Nolen-Hoeksema, R. C., and L. J. Ruff. (2001). Moment tensor inversion of microseisms from the B-sand propped hydrofracture, M-site, Colorado. Tectonophysics, 336(1-4), 163–181. doi: **https://doi.org/10.1016/S0040-1951(01)00100-7**

Pettitt, W., M. Pierce, B. Damjanac, J. Hazzard, L. Lorig, C. Fairhurst, I. Gil, M. Sanchez, N. Nagel, J. Reyes-Montes, *et al.* (2011). Fracture network engineering for hydraulic fracturing. The Leading Edge, 30(8), 844-853. doi: **https://doi.org/10.1190/1.3626490**

Psencık, I., and T. N. Teles. (1996). Point source radiation in inhomogeneous anisotropic structures. Pure and Applied Geophysics, 148, 591–623. doi: **https://doi.org/10.1007/BF00874581**

Shi, Z., and Y. Ben-Zion. (2009). Seismic radiation from tensile and shear point dislocations between similar and dissimilar solids. Geophysical Journal International, 179(1), 444-458. doi: **https://doi.org/10.1111/j.1365-246X.2009.04299.x**

Sıleny, J., D. P. Hill, L. Eisner, and F. H. Cornet. (2009). Non–double-couple mechanismsˇ of microearthquakes induced by hydraulic fracturing. Journal of Geophysical Research, Solid Earth, 114(B8). doi: **https://doi.org/10.1029/2008JB005987**

Sıleny, J., and A. Milev. (2008). Source mechanism of mining induced seismic events—resolution of double couple and non double couple models. Tectonophysics, 456(1-2), 3–15. doi: **https://doi.org/10.1016/j.tecto.2006.09.021**

Stefanov, Y. P. (2008). Numerical modeling of deformation and failure of sandstone specimens. Journal of Mining Science, 44, 64–72. doi: **https://doi.org/10.1007/s10913-008-0006-1**

Stefanov, Y. P., M. A. Chertov, G. R. Aidagulov, and A. V. Myasnikov. (2011). Dynamics of inelastic deformation of porous rocks and formation of localized compaction zones studied by numerical modeling. Journal of the Mechanics and Physics of Solids, 59(11), 2323–2340. doi: **https://doi.org/10.1016/j.jmps.2011.08.002**

Wang, H., M. Marongiu-Porcu, and M. J. Economides. (2016). Poroelastic and poroplastic modeling of hydraulic fracturing in brittle and ductile formations. SPE Production & Operations, 31(01), 47–59. doi: **https://doi.org/10.2118/168600-PA**

Warpinski, N. R. (2013). Understanding hydraulic fracture growth, effectiveness, and safety through microseismic monitoring. [Conference paper]. ISRM International Conference for Effective and Sustainable Hydraulic Fracturing, International Society for Rock Mechanics, Brisbane, Australia.

Wilkins, M. L. (1999). Computer simulation of dynamic phenomena. Springer Science.

Zangeneh, N., E. Eberhardt, and R. M. Bustin. (2014). Investigation of the influence of natural fractures and in situ stress on hydraulic fracture propagation using a distinct-element approach. Canadian Geotechnical Journal, 52(7), 926–946. doi: **https://doi.org/10.1139/cgj-2013-0366**

Zoback, M. D. (2010). Reservoir geomechanics. Cambridge University Press.